Comparative analysis of carbon dioxide and hydrogen plume migration in aquifers inspired by the FluidFlower benchmark study

Misaghi Bonabi, Amin; van Rooijen, Willemijn; Al Kobaisi, Mohammed; Vuik, Cornelis; Hajibeygi, Hadi

DOI
10.1016/j.ijhydene.2025.04.401

Publication date
2025

Document Version
Final published version

Published in
International Journal of Hydrogen Energy

International Journal of Hydrogen Energy 135 (2025) 56–68

Contents lists available at ScienceDirect

International Journal of Hydrogen Energy

journal homepage: www.elsevier.com/locate/he

Comparative analysis of carbon dioxide and hydrogen plume migration in aquifers inspired by the FluidFlower benchmark study

Amin Misaghi Bonabi [a,*], Willemijn van Rooijen [b], Mohammed Al Kobaisi [a], Cornelis Vuik [a], Hadi Hajibeygi [b]

[a] Department of Applied Mathematics, Faculty of Electrical Engineering, Mathematics, and Computer Science, Delft University of Technology, Delft, The Netherlands
[b] Department of Geoscience and Engineering, Faculty of Civil Engineering and Geosciences, Delft University of Technology, Delft, The Netherlands

ARTICLE INFO

Keywords:
Underground hydrogen storage
Geological carbon dioxide storage
Flow in porous media
Simulation
Trapping
Multiphase flow

ABSTRACT

Large-scale geological storages of hydrogen (H_2) and carbon dioxide (CO_2) in saline aquifers present feasible options for a sustainable energy future. We compared the plume migration of CO_2 and H_2 in aquifers using the FluidFlower benchmark, incorporating the state-of-the-art thermophysical and petrophysical properties. The H_2 plume, with its higher buoyancy and mobility compared to CO_2, remains predominantly in the gas phase due to its lower solubility, increasing the chances of escaping through fractures or migration to distant regions. This additionally leads to a higher pressurized reservoir, which, along with higher buoyancy, increases the chance of caprock penetration. Dissolution trapping of CO_2 into brine increases over time due to its fingering, while H_2 does not show fingering. Our findings show that while geological carbon storage (GCS) benefits significantly from all structural, dissolution, and residual trapping, underground hydrogen storage (UHS) relies mainly on structural trapping, making the integrity of sealing elements of the system a key factor in its performance.

1. Introduction

Reaching a sustainable energy future with the growing global energy demand to limit anthropogenic warming to under 2 °C requires a transition away from fossil fuels, capture and safe storage of gigatons of carbon dioxide (CO_2), and large-scale energy storage in geological formations [1]. Geological carbon dioxide storage (GCS) has been a key to climate strategies since 1995, focusing on capturing emissions from hard-to-decarbonize industries, compressing and transporting CO_2, and injecting it into deep geological formations for permanent storage [2,3].

Furthermore, the transition to renewable energy sources requires large-scale energy storage solutions to balance production and demand on a seasonal scale. Hydrogen, H_2, with its high gravimetric energy density of about 33 $kWh\,kg^{-1}$ and clean combustion byproducts, is emerging as a key energy carrier for this purpose [4,5]. However, its low density requires enormous storage volumes to achieve TWh-scale capacity. Underground geological formations provide the necessary volume capacity for large-scale H_2 storage, i.e., UHS, and are estimated to be significantly more cost-effective compared to other industrial solutions like liquefied hydrogen storage or high-pressure tank storage [6–8].

There are two main categories of underground gas storage: porous media and cavern storage, with options such as depleted hydrocarbon reservoirs, aquifers, and salt caverns. The globally available aquifers offer significant volume potential for UHS. Successful aquifer storage relies on a well-suited geometry for structural trapping, a favorable range of porosity and permeability for efficient injection-production cycles and reliable seals to prevent gas migration [9]. Other challenges to be resolved include the risks of biochemical reactions and hydrogen interactions with reservoir minerals [10].

On the hydrodynamic aspect, when H_2 is injected into an aquifer, it increases the reservoir pressure, displaces water away, and tends to migrate upward. This process introduces several reservoir management challenges, including ensuring caprock integrity, maintaining the recoverability and purity of H_2, monitoring H_2 plume migration, and managing induced seismicity due to the stress alterations within and outside the reservoir region. The complexity of these issues is further amplified by geological heterogeneity, subsurface uncertainties, and the cyclic (and hysteretic) nature of the storage [11].

Accurate and reliable simulations of H_2 flow in porous aquifers are essential for UHS feasibility, performance optimization and managing its associated risks. These simulations require modeling two-phase (nonwetting and wetting) two-component (H_2 and brine) flow and transport in porous media. Here, for the sake of plume migration analyses, we assume no other gas is present, and that H_2 can be

* Corresponding author.
E-mail address: A.MisaghiBonabi@tudelft.nl (A. Misaghi Bonabi).

https://doi.org/10.1016/j.ijhydene.2025.04.401
Received 7 February 2025; Received in revised form 17 April 2025; Accepted 23 April 2025
Available online 8 May 2025

injected directly into the aquifer. Reliability of this multiphase multi-component flow simulation depends on reliable estimations of petrophysical functions, such as capillary pressure, relative permeability, and residual saturation [12,13] as well as accurate representations of the thermodynamic behavior of the H_2/brine system [14–17].

Petrophysical properties for H_2-brine-rock systems have been the focus of several experimental studies in the recent literature. At bubble scale, wettability analyses indicated that the H_2-brine-rock systems remain strongly water wet for sandstone reservoirs [18,19], with the intrinsic angles ranging from 21° to 43°. Moreover, microfluidic dynamic studies revealed the hysteretic nature of the cyclic transport of H_2 in microchannels, due to the reported differences between its advancing and receding contact angles [14,20]. Furthermore, interfacial tension (IFT) of H_2-brine-rock systems was found to decay slightly with increasing the pressure (at moderate temperatures), e.g., at 298 K, IFT decreases from 72.3 mN m^{-1} to 68.7 mN m^{-1} as pressure rises from 1 MPa to 45 MPa. However, IFT was found to be a strong function of temperature, e.g., it decreased from 72.3 mN m^{-1} at 298 K to 59 mN m^{-1} at 372 K [21–24]. At core-scale, importantly, effective relative permeability and capillary pressure functions have been directly measured by several researchers under x-ray CT imaging [25–30] and without CT imagining [31,32]. These studies revealed the intrinsic hysteretic nature of the transport functions, as well as the residual trapping volumes. In particular, the nearly 20% trapped of H_2 after the first cycle is confirmed by different researchers [25,26]. Outside the scope of this work, yet important to note, is that microbial impacts on H_2 transport are still under systematic investigations [33–35]. Moreover, it is also important to emphasize that micro-scale simulations and upscaling their results to core scale are crucial to develop a robust understanding of H_2 transport across different conditions [36,37].

Field-scale simulations have focused on homogeneous reservoirs [38], monotonic H_2 injection [39] or cyclic injection using commercial simulators with approximate petrophysical functions [40–43] or accurate lab-based functions [41]. A comparative analysis between the plume migration for CO_2 and H_2 significantly helps to realize in what ways the UHS performance is more sensitive than GCS. Moreover, CO_2 is one of the options for cushion gas in UHS [44,45]. As such, studying how different the two fluids transport in reservoirs becomes even more crucially important. For such a comparative analysis, it is important to consider reliable input parameters to describe the fluids and their interactions with the rock, as well as meaningful geological heterogeneity and trapping mechanisms [46].

The recent FluidFlower benchmark offers a robust foundation for CO_2 flow simulation, providing a meticulously validated framework that integrates both experimental and computational analyses [47]. Building upon this established system, we extend its application to UHS by employing the same geological configuration for simulating H_2 flow. This enables a direct and systematic comparison of CO_2 and H_2 plume migration in porous media. By leveraging the benchmark's reliability, we investigate the key differences in fluid behavior, migration patterns, and storage dynamics between the two gases, highlighting the contrasting physical mechanisms that govern GCS and UHS operations. Comparing CO_2 transport, which has a high density, viscosity, and solubility, to H_2, which is quite the opposite, provides a critical perspective on two distinct cases of gas flow dynamics and storage in porous media, their differences in trapping mechanisms, and the caprock integrity facing different gases.

A fully-implicit finite-volume-based simulation framework is used for multi-phase and multi-component flow in porous media, which allows for hysteretic simulations in a heterogeneous reservoir. Thermodynamics properties are taken from the state-of-the-art density and solubility functions formulated using equations of state calibrated with empirical data collected across diverse conditions. H_2 viscosity is computed using the friction theory. All the implementations have been done in the open-access DARSim simulator [48]. We quantify the performance differences between the two cases by measuring the spatial distribution of injected gases in wetting and nonwetting phases, reporting pressure at critical regions of the domain, and comparing the mass fractions of CO_2 and H_2 in different states.

This manuscript is structured as follows. The governing equations and thermophysical models are presented in Section 2. Section 3 studies the simulation results and comparison of plume migration of H_2 and CO_2 at standard conditions, reservoir conditions, and cyclic storage. Section 4 presents practical insights into the site selection and risk management based on the results of this comparative analysis. Finally, concluding remarks are presented in Section 5.

2. Physical models and methods

2.1. Thermophysical properties of H_2 and CO_2

This section explores the thermophysical properties of H_2 and CO_2, including density, viscosity, and solubility. These properties are analyzed and derived using appropriate thermodynamic equations of state, supported by accurate and reliable experimental data and computational simulations.

2.1.1. Density and viscosity

Fig. 1(a) shows the density of H_2 and CO_2 as a function of pressure for both standard condition temperature (20 °C) and reservoir temperature (50 °C). For H_2 densities, the Peng–Robinson Equation of State [49] is used, in combination with the volume-shift method [50,51]. For CO_2 densities, a modified Redlich–Kwong equation is used, as proposed in the literature [52]. Although fixed viscosity values are used in the simulations of this article, Fig. 1(b) provides a comparison of H_2 viscosity with CO_2 as a function of pressure. H_2 viscosity is computed using the friction theory [53,54], and CO_2 viscosity is taken from REFPROP [55].

Note that both CO_2 and H_2 reach a supercritical state under reservoir pressure and temperature, however, CO_2 exhibits a notable change in behavior when transitioning to the supercritical phase, as shown in Fig. 1. CO_2 has a critical temperature of $T_C = 31$ °C and a critical pressure of $P_C = 74$ bar, while H_2 has a much lower critical temperature of $T_C = -240$ °C and critical pressure of $P_C = 13$ bar [55]. Consequently, CO_2 is 58 times denser and 7 times more viscous than H_2 under reservoir conditions (50 °C, 100 bar). As a result, the CO_2 plume is expected to flow more slowly than the H_2 plume in subsurface environments.

2.1.2. Solubility

The solubility of gases in brine is influenced by various factors, including chemical characteristics, pressure, temperature, and brine salinity. The quantity of dissolved gas in the liquid phase is characterized by the volume of gas that dissolves per unit volume of liquid [56], i.e.,

$$R_s = \frac{\rho_b^{STC} x_{i,w}}{\rho_i^{STC}(1 - x_{i,w})}, \tag{1}$$

where b, w, and STC denote brine, wetting phase, and standard conditions, respectively, and i is either CO_2 or H_2 depending on which system (GCS or UHS) is being studied. Physically, R_s represents the volume that the dissolved gas would occupy if brought to the surface conditions.

To model the solubility of CO_2-brine and H_2-brine systems, thermodynamic models have been developed in the literature based on empirical data obtained under a wide range of conditions. In this study, the procedure by Spycher et al. [52], and validated by Wang et al. [57], is used to determine the solubility of the CO_2-brine system. For the H_2-brine system, however, the thermodynamic model of Shabani and Vilcáez [58] is used, which is an extension of the model proposed by Ziabakhsh-Ganji and Kooi [51]. It is worth to be highlighted that the

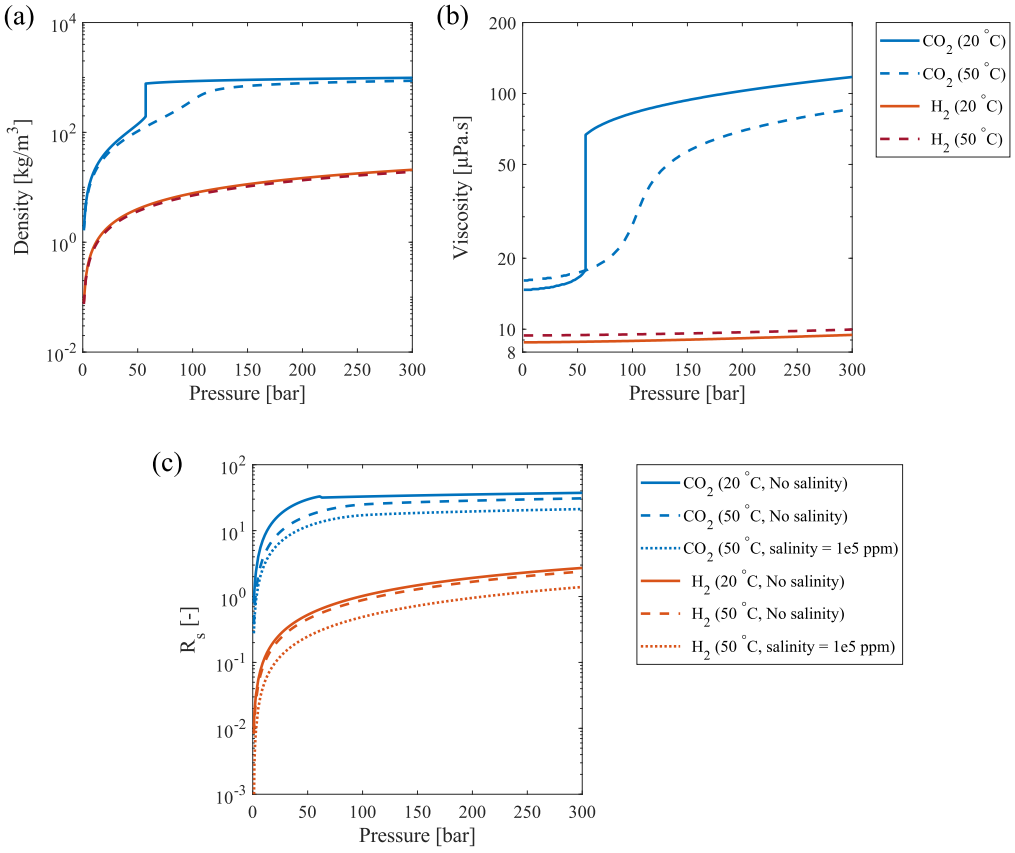

Fig. 1. (a) Density, (b) Viscosity, and (c) Solubility of CO_2 and H_2 as a function of pressure at temperatures of 20 °C and 50 °C.

recent studies have demonstrated that the thermodynamics models Shabani and Vilcáez [58] can be indeed validated by experimental [59,60] and molecular dynamics simulation results [14,61].

The dissolution of CO_2 and H_2 in pure water is derived as a function of pressure and salinity, which is shown in Fig. 1(c). Under standard temperature and pressure conditions, the solubility of CO_2 is approximately 76 times higher than that of H_2. However, as pressure increases, this difference reduces. In reservoir conditions, the solubility ratio decreases to 17. Brine salinity significantly reduces the solubility of gases, as shown in Fig. 1(c). For example, brine in reservoir conditions with a salinity of 1×10^5 ppm NaCl can dissolve 31% less CO_2 and 45% less H_2 compared to distilled water.

2.2. Governing equations of fluid flow in porous media

In order to have a precise comparison of plume migration, generalized mass conservation equations of components are employed for both CO_2-brine and H_2-brine 2-component, 2-phase systems as

$$\sum_{\alpha=w,n}\left[\frac{\partial}{\partial t}(\phi s_\alpha \rho_\alpha x_{c,\alpha}) + \nabla\cdot(\boldsymbol{u}_\alpha \rho_\alpha x_{c,\alpha} + \rho_\alpha \boldsymbol{j}_{c,\alpha}) - q_\alpha x_{c,\alpha}\right] = 0, \tag{2}$$

where the subscriptions α denotes phases, i.e., $\alpha \in \{wetting, nonwetting\}$, and c denotes components, $c \in \{CO_2, brine\}$ for CO_2-brine system and $c \in \{H_2, brine\}$ for H_2-brine system. Moreover, ϕ is the porosity of the medium, s_α, ρ_α, and q_α are saturation, density, and source term of phase α, respectively. u_α and $j_{c,\alpha}$ are velocity of phase α and diffusion flux of component c in phase α, and $x_{c,\alpha}$ is the mass fraction of component c in phase α. Darcy velocity relation is employed as follows for the velocity of the phase α, i.e.,

$$\boldsymbol{u}_\alpha = -\frac{k_{r,\alpha}\mathbf{k}}{\mu_\alpha}\left(\nabla p_\alpha - \rho_\alpha \boldsymbol{g}\right), \tag{3}$$

where $\mathbf{k}$, μ_α, and p_α are the intrinsic permeability of rock, the viscosity of the phase α, and the pressure of phase α. $k_{r,\alpha}$ is the relative permeability of the phase α. The phase pressures are related by capillary pressure, i.e., $p_c = p_n - p_w$.

Both relative permeability and capillary pressure are hysteretic functions of saturation. The fact that their values—$k_{r,\alpha}$ and p_c—differ depending on whether the system is undergoing drainage or imbibition is known as hysteresis. The difference arises because drainage is dominated by the smaller pores, whereas imbibition is dominated by the larger pores [62]. Hysteresis is essential for accurately addressing the residual trapping in the system, especially in cyclic storages. At any given point in the reservoir, once it has undergone the initial drainage, a transition to imbibition results in a decrease in gas saturation, during which a portion of the gas becomes immobilized as residual gas. However, in subsequent drainage cycles, if the gas saturation exceeds the previously reached maximum, the trapped gas can become reconnected and mobilized. In this work, the hysteretic functions for both GCS and UHS are simulated using the recently developed methodology in the literature [57,63].

Diffusion flux of component c in phase α is proportional to the gradient of concentration according to Fick's law, i.e.,

$$\boldsymbol{j}_{c,\alpha} = -\phi S_\alpha D_{c,\alpha}\nabla x_{c,\alpha}, \tag{4}$$

where $D_{c,\alpha}$ is the diffusion coefficient.

The nonlinear system of equations is solved using finite volume discretization in space and implicit discretization in time, with the Newton–Raphson method is employed for linearization. Wetting phase pressure (P_w) and the total mole fraction of the first component (z_c; where c = CO_2 or H_2) are set as primary variables for the system, where $z_c = \sum_\alpha(x_{c,\alpha}\rho_\alpha S_\alpha / \sum_\alpha(\rho_\alpha S_\alpha))$.

In a two-phase state, the liquid phase is assumed to be fully saturated. Thus, the amount of dissolution can be extracted from predefined

Table 1
Petrophysical parameters of different sand types of FluidFlower benchmark.

Name	K_x [m^2]	K_z [m^2]	ϕ	$S_{i,w}$	$k_{r,w}$	$S_{i,n}$	$k_{r,n}$	$p_{c,\ entry}$ [Pa]
G	4.31E−09	4.79E−09	0.46	0.10	0.75	0.06	0.16	0
F	1.92E−09	2.13E−09	0.43	0.12	0.72	0.13	0.11	0
E	9.02E−10	1.00E−09	0.45	0.12	0.93	0.06	0.10	0
D	5.00E−10	5.55E−10	0.44	0.12	0.95	0.08	0.02	98
C	2.13E−10	2.37E−10	0.43	0.14	0.93	0.10	0.05	294
ESF	1.98E−11	2.20E−11	0.44	0.32	0.71	0.14	0.09	1471
Barrier	4.50E−19	5.00E−19	0.001	0.32	0.71	0.14	0.09	0

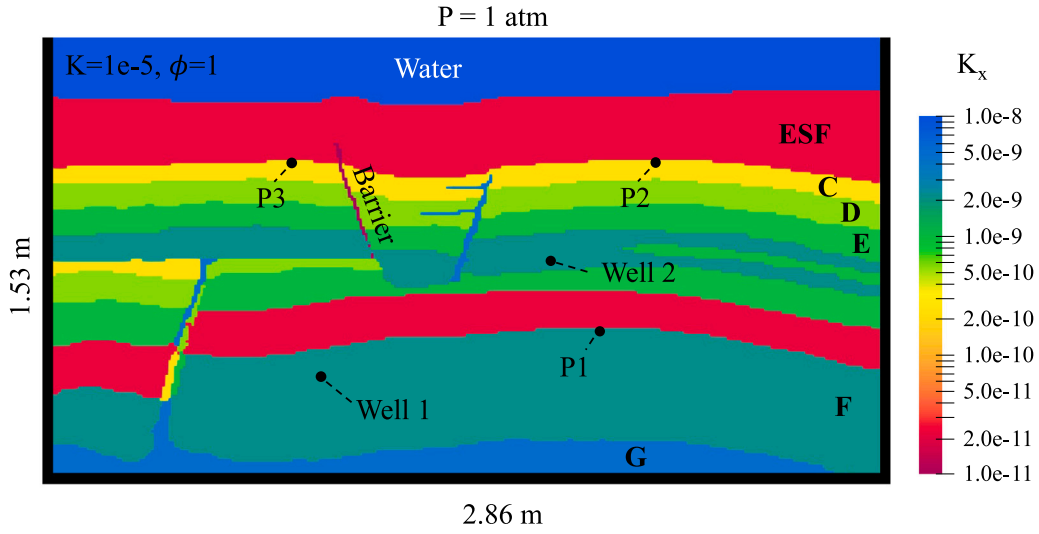

Fig. 2. Geometry, boundary conditions and horizontal permeability distribution, K_x, of FluidFlower benchmark. P1, P2, and P3 are reference points for the results.

R_s curves. If the system is in a single-phase state, i.e., $\sum_c z_c K_c - 1 < 0$ holds, R_s is calculated based on the existing amount of moles of solute [57], i.e.,

$$R_s = \frac{\rho_b^{STC} z_i}{\rho_i^{STC}(1 - z_i)}. \tag{5}$$

Here, z_c and K_c are total mole fraction of component c, and the phase equilibrium ratio, respectively.

3. Results and discussion

In this section, the plume migration of CO_2 and H_2 under varying conditions is analyzed through simulations conducted using DARSim (Delft Advanced Reservoir Simulator) [48]. The study begins with the reconstruction and assessment of the FluidFlower benchmark [47], an experimental–numerical multiphase flow study originally designed for CO_2 injection, to evaluate plume migration at standard conditions. Following this, a scaled version of the FluidFlower is modeled under realistic reservoir conditions to investigate plume dynamics at field-relevant scales. Finally, a cyclic injection and production scheme is simulated to explore the behavior of H_2 during storage operations.

3.1. Plume migration at standard conditions

Under standard conditions (20 °C, 1 bar), CO_2 and H_2 exhibit significant differences in density, viscosity, and solubility, affecting their flow pattern. CO_2 has a density of 1.82 kg m^{-3}, which is approximately 20 times higher than H_2's density of 0.09 kg m^{-3}; similarly, CO_2's viscosity is 17.7 μ Pa s, nearly double that of H_2, which has a viscosity of 8.8 μ Pa s, indicating that CO_2 has greater internal resistance to flow. The most striking difference lies in their solubility in water: CO_2 has a solubility (Rs) of 0.81, vastly exceeding H_2's solubility of 0.01.

In order to construct an acceptable comparison, we focus on the FluidFlower benchmark. It features a well-characterized porous medium, mimicking geological reservoir properties, with precisely controlled boundary and initial conditions to enable detailed comparisons between experiments and simulations. In this section, the FluidFlower framework is adapted to evaluate the migration of the CO_2 plume, utilizing its validated numerical models [63] to assess the unique flow characteristics of H_2 under similar conditions.

The problem setup involves a 2D box measuring 1.53 m in height, 2.86 m in length, and 1.9 cm in width, filled with seven distinct soil types to represent realistic geological formations, including a barrier and fractures. Two low-permeability layers, modeled as ESF soil, serve to mimic the effect of a cap rock. The top boundary of the box is filled with water maintained at a constant height and is open to flow under atmospheric pressure, which is modeled as a porous medium with porosity of $\phi = 1$ and a very high permeability of $k = 1 \times 10^{-5}$ m^2. The other three boundaries are sealed as no-flow conditions. Two injection wells are used to inject pure CO_2 and H_2 at a constant rate of 1.44×10^{-4} m^3 s^{-1}. The first well injects continuously from the start of the simulation for 5 h, while the second well begins at 2.25 h and continues for 2.75 h. The simulations are done under isothermal conditions of 20 °C and continue for 2 days. Material properties of the layers are detailed in Table 1, and Brooks–Corey functions with a shape parameter of $\lambda = 2$, and hysteresis effects are employed to model relative permeability and capillary pressure relationships. The diffusion coefficient is 1×10^{-9} m^2 s^{-1} all over the domain. The geometry and boundary conditions of the problem are shown in Fig. 2. Fig. 3 shows the relative permeability and capillary pressure curves of the FluidFlower benchmark.

Fig. 4 illustrates the evolution over time of the spatial distribution of nonwetting phase saturation and dissolution of CO_2 and H_2. While the overall saturation field exhibits a similar pattern in both cases, notable differences emerge in the extent of plume migration. H_2 gas occupies a significantly larger portion of the domain, particularly in the top-left region of the box near P3. This difference can be attributed to CO_2's much higher solubility—approximately 75 times greater than

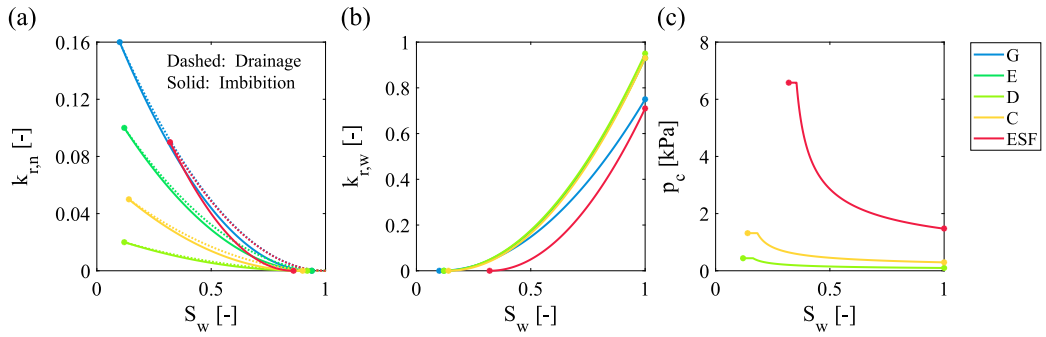

Fig. 3. (a) Relative permeability of nonwetting phase, $k_{r,n}$, (b) relative permeability of wetting phase, $k_{r,w}$, (c) and capillary pressure, p_c, of the FluidFlower benchmark. Different colors correspond to different layers, as shown in Fig. 2.

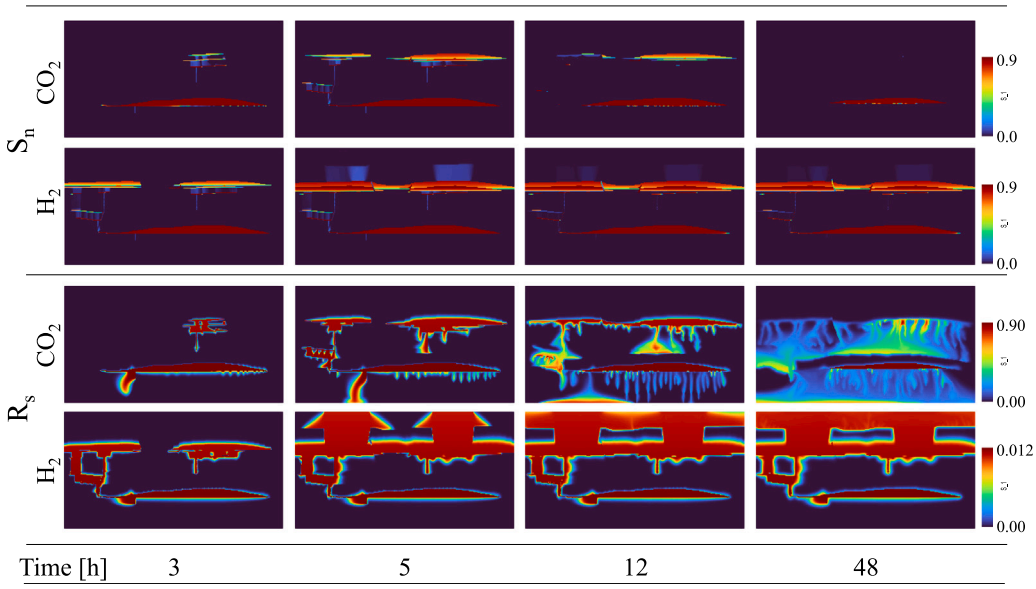

Fig. 4. A comparison between the evolution over time of the spatial distribution of nonwetting phase saturation, S_n, and dissolution, R_s, for the CO_2 and H_2 cases at standard conditions.

H_2 at standard conditions—which causes substantial dissolution during plume migration. As CO_2 dissolves extensively, its gas plume is unable to occupy the domain greatly, unlike H_2, which dissolves less in aqueous phase and remains predominantly in the gaseous phase and consequently occupies more space. This behavior leads to generally higher pressures in the H_2 case compared to the CO_2 case, as depicted in Fig. 5(a). The higher pressure enables the H_2 plume to overcome capillary barriers imposed by low-permeability layers, a phenomenon particularly evident at T = 5 h in Fig. 4.

Although the saturation fields of CO_2 and H_2 share similarities, their dissolution patterns are very different. The larger spatial distribution of the H_2 gas plume leads to a more dispersed dissolution field, despite the relatively low amount of dissolved H_2. Escaped H_2 also dissolves into the overlying water layer, saturating it with H_2. In contrast, CO_2's significantly higher solubility and density induces density-driven flows, or "fingering", within the wetting phase (Fig. 4). These flows result in the downward movement of denser water with dissolved CO_2. As it sinks, it creates room for further dissolution; this ongoing process is evident in the simulation: the top-right CO_2 plume near P2 and P3 dissolves completely by the end of the simulation, while the bottom plume near P1 thins over time. In comparison, dissolved H_2 remains stationary and does not exhibit such vertical movement. Consequently, the dissolution process for CO_2 is continuous, reducing pressure over time (Fig. 5(a)), whereas the H_2 system quickly reaches a steady state.

Fig. 5(b) illustrates the mole quantities within a single grid block (1 cm × 1 cm) near points P1, P2, and P3 in both the wetting and nonwetting phases. The data reveal stark differences between CO_2 and H_2 behavior. The amount of H_2 in the wetting phase is minimal across all points, whereas the amount of dissolved CO_2 is significant. Furthermore, H_2 behavior is steady over time; once the H_2 plume reaches these points, no notable changes occur. In contrast, CO_2 exhibits transient behaviors in both phases. As the CO_2 plume reaches a point, the mole quantity in both phases increases. A sudden decrease in the nonwetting-phase CO_2 is observed as water, carrying dissolved CO_2, is displaced by the gas-phase CO_2. Subsequently, the amount of dissolved CO_2 in the wetting phase gradually increases due to ongoing dissolution. This process continues until the gas-phase CO_2 is depleted, after which the dissolved CO_2 in the wetting phase also begins to decrease. At P1, the mole quantities of both CO_2 and H_2 increase with injection and then stay constant, as the area around P1 becomes saturated with either gas. Another notable observation is the delay between the arrival of the CO_2 and H_2 plumes at the points. H_2 reaches the points faster, whereas CO_2 moves slowly and dissolves significantly during its migration, delaying its arrival.

Fig. 6 shows the mass fraction distribution of CO_2 and H_2 within the box relative to the total injected mass. The escaped mass is determined by subtracting the total mass of CO_2 or H_2 remaining inside the box from the total injected amount. For CO_2, most of the mass is dissolved and continues to dissolve over time. In contrast, H_2 predominantly remains in the gas phase, accounting for 70.7% of its total mass, with 0.3% of this mass becoming immobile and 4.3% dissolved. Notably,

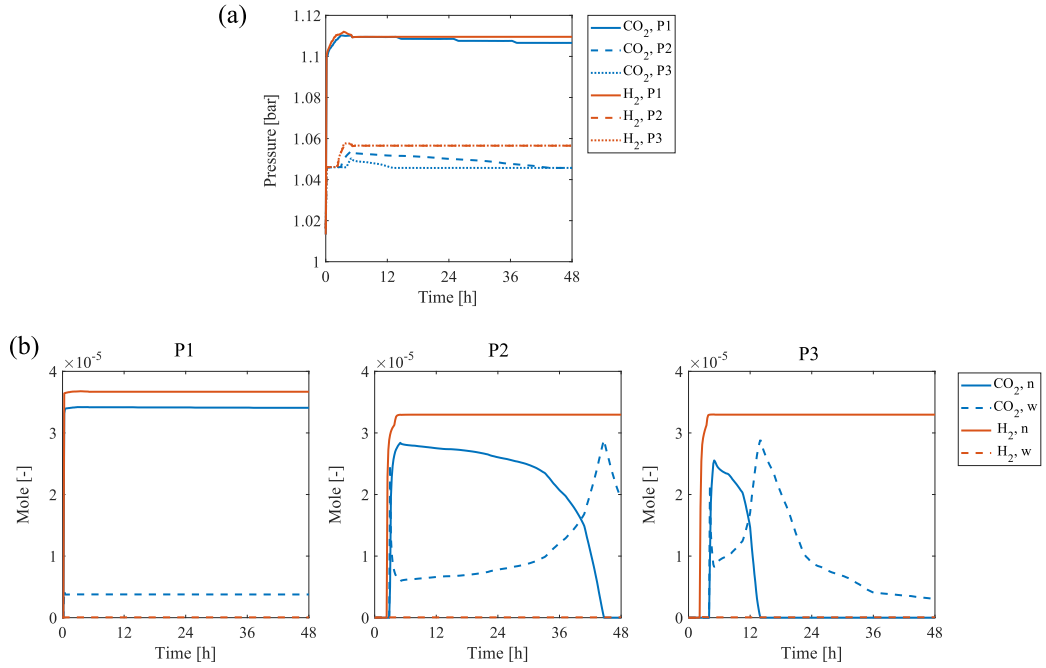

Fig. 5. A comparison between (a) the nonwetting phase pressure, p_n, and (b) mole amount in wetting phase (w) and nonwetting phase (n) in the neighborhood of 1 cm of points P1, P2, and P3 for the CO_2 and H_2 cases at standard conditions.

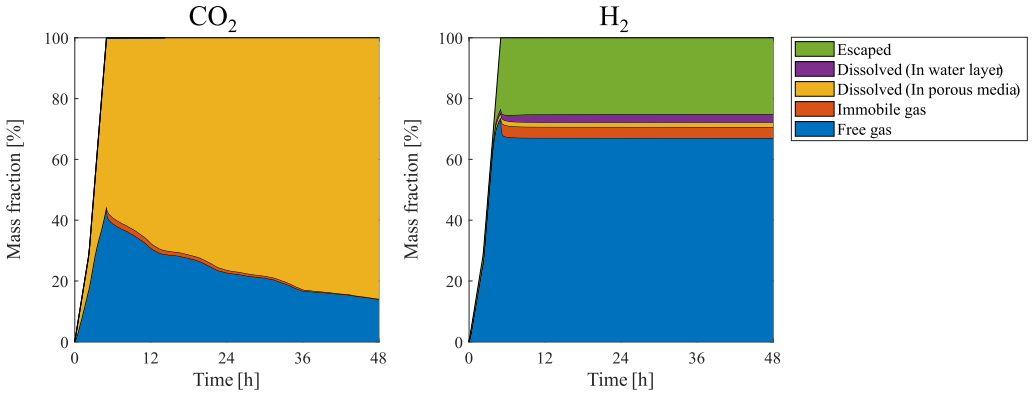

Fig. 6. A comparison of the mass fraction distribution of CO_2 and H_2 with respect to total injected mass at standard conditions.

25% of the injected H_2 escapes the box during the period close to the end of the injection, driven by a significant pressure increase towards the end of the injection period.

3.2. Plume migration at reservoir conditions

Performing simulations at reservoir conditions is essential to accurately capture the behavior of CO_2 and H_2 in the subsurface, where temperature and pressure differ significantly from standard conditions. At 150 bar and 50 °C, the density, viscosity, and solubility (Rs) of CO_2 are 671.7 kg m^{-3}, 51.4 μ Pa s, 27.01, respectively. For H_2, these values are 11.02 kg m^{-3}, 9.6 μ Pa s, 1.29. These differences highlight how reservoir conditions modify the disparity in physical properties between CO_2 and H_2. Simulating reservoir conditions ensures that the models reflect the real-world physical and chemical interactions critical for safe and effective subsurface storage.

The FluidFlower benchmark is scaled to simulate a realistic reservoir. Adjustments included removing the top water layer and scaling the box dimensions by a factor of 1000, resulting in a small aquifer with a depth of 1.29 km and a length of 2.86 km; width of the problem is assumed 1 m. Permeabilities across all layers are reduced by a factor of 20, except for the ESF layer, which is reduced by a factor of 200 to represent a more restrictive caprock. The vertical-to-horizontal permeability ratio is set to 0.5, reflecting the anisotropic nature of subsurface strata, which are typically more permeable horizontally. The geometry and boundary conditions of the problem are shown in Fig. 7. Relative permeabilities are kept unchanged due to the lack of conclusive literature on scaling these properties. The capillary entry pressure for CO_2 is calculated using Leverett J-functions and experimental data suggested by Abdoulghafour et al. [64], expressed as $p_{\text{entry, CO}_2} = \sqrt{\phi/K_x}\, 6.12 \times 10^{-3}$ Pa. For H_2, Leverett J-function of CO_2 is scaled based on the ratio of interfacial tensions between H_2 and CO_2. As supported by several experiments reported in Mouallem et al. [22], while the interfacial tensions of CO_2 and H_2 is "approximately" at the same range in standard conditions, the interfacial tension of CO_2 decreases significantly with pressure (approximately 57% from 1 bar to 150 bar), whereas the interfacial tension of H_2 remains relatively constant. As a result, we estimated the capillary pressure for the H_2 case to be approximately 2.33 times that of the CO_2 case for each layer. As a result, under these conditions, the Bond number of H_2 is approximately 1.3 times higher than that of CO_2. The diffusion coefficient and water compressibility are set to 1×10^{-9} m^2 s^{-1} and 4×10^{-10} Pa^{-1}, respectively.

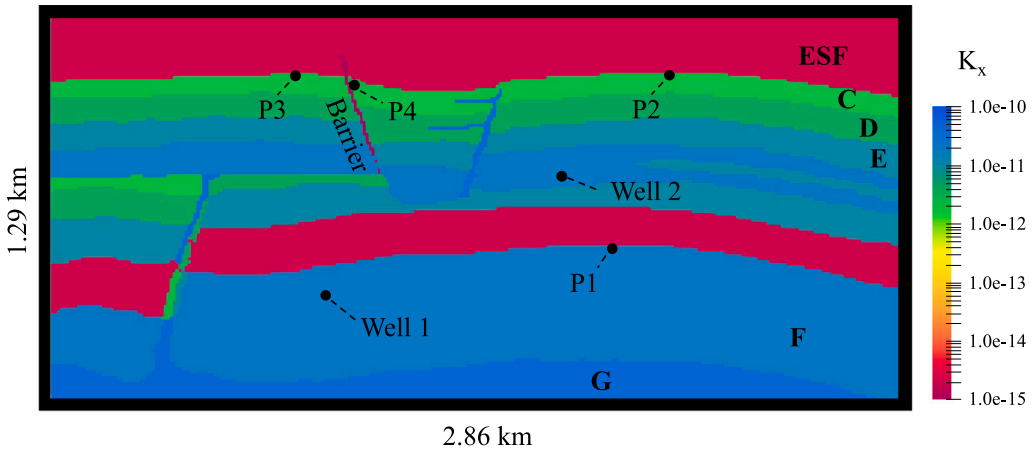

Fig. 7. Geometry, boundary conditions and permeability distribution, K_x, of the reservoir conditions problem. P1–P4 are reference points for the results.

Table 2
Petrophysical parameters of different sand types of FluidFlower benchmark.

Name	K_x [m^2]	K_z [m^2]	ϕ	$p_{entry,\ CO_2}$ [Pa]	$p_{entry,\ H_2}$ [Pa]
G	4.0E−11	2.0E−11	0.35	5.7E+02	1.3E+03
F	2.0E−11	1.0E−11	0.25	6.8E+02	1.6E+03
E	1.0E−11	5.0E−12	0.20	8.7E+02	2.0E+03
D	4.0E−12	2.0E−12	0.20	1.4E+03	3.2E+03
C	2.0E−12	1.0E−12	0.20	1.9E+03	4.5E+03
ESF	2.0E−15	1.0E−15	0.10	4.3E+04	1.0E+05
Barrier	1.0E−21	5.0E−22	0.001	–	–

The reservoir model assumes no-flow boundary conditions at all boundaries. The initial reservoir pressure is set to 100 bar at the top boundary, increasing hydrostatically based on water density. The domain is discretized into 1 m × 1 m cells. To prevent unphysical pressure buildup and emulate a realistic semi-infinite reservoir, additional pore volume is assigned to the boundary cells of the left and right boundaries (not applied to the caprock layer (ESF)), allowing fluids to flow laterally beyond the simulated region and prevent unrealistic excessive pressure build-up. Specifically, the pore volume of these boundary cells is increased by a factor of 5000, representing an effective reservoir extension of 5 km beyond the region of interest on each side. The reservoir is modeled under isothermal conditions, maintaining a temperature of 50 °C. Two injection wells are utilized to inject pure CO_2 and H_2 at a constant rate of 5.8 $m^3\ s^{-1}$. The first well operates continuously from the start of the simulation for a duration of four months, while the second well begins injection after two months and continues for two months. In order to compare the spatial distribution of the plume migrations in both cases, it is assumed that the same volume of CO_2 and H_2 are injected into the reservoir (due to the greater density of CO_2, it would be difficult to visually discern if the injection of the same mass (or mole) of CO_2 and H_2). Over the total injection period, 7.01×10^4 ton of CO_2 and 1.19×10^3 ton of H_2 are injected into the reservoir. The injection rate is intentionally assigned high, with a total mole fraction of water to CO_2 and water to H_2 of 22:1 and 64:1, respectively, to accelerate plume migration. Simulations span a period of five years. Material properties of the reservoir layers are outlined in Table 2.

Fig. 8 illustrates the evolution over time of the spatial distribution of nonwetting phase saturation and dissolution of CO_2 and H_2. Unlike the problem at standard conditions, where the plume shapes were similar, the plume behavior here is distinctly different due to the significant density contrast between CO_2 and H_2. The much higher density of CO_2 leads to reduced buoyancy forces compared to H_2, causing the CO_2 plume to spread more evenly in all directions, while the H_2 plume rises rapidly and tends to accumulate horizontally under the cap rock. The higher density of CO_2 also results in slower plume migration compared to H_2. For instance, it takes CO_2 approximately 16 months to reach point P2, whereas H_2 reaches the same location in just 3 months. Similarly, it takes CO_2 more than 5 years to reach point P3, while H_2 arrives there within 3.5 months. Another notable consequence of H_2's higher buoyancy is its greater penetration into the caprock. Despite the capillary entry pressure for the CO_2 case being 2.33 times lower than that of H_2, and the total injected mass (or mole) of CO_2 being 60 times greater than H_2, the H_2 plume penetrates further into the caprock. This behavior is clearly visible in the nonwetting phase saturation at 60 months, where H_2 exhibits more pronounced upward migration into the caprock compared to CO_2.

Fig. 9 shows the pressure evolution at points P1, P2, and P3, indicating a general increase of approximately 50% compared to initial pressure. The pressures at P2 and P3 are similar for both CO_2 and H_2 cases; however, at P1, the CO_2 case exhibits higher pressure values compared to H_2. This difference arises because H_2 quickly escapes through the fracture on the right side of the domain, preventing significant pressure buildup beneath the caprock. In contrast, CO_2 accumulates under the caprock, causing a more pronounced pressure increase at P1. Over time, the pressure in the CO_2 case gradually decreases as CO_2 slowly escapes through the fracture, leading to a more prolonged pressure dissipation process compared to H_2.

Fig. 10(a) presents the mass fraction distribution of CO_2 and H_2 within the domain relative to the total injected mass. The "Escaped" label represents the amount of CO_2 or H_2 that has migrated into the right and left boundary cells, where the pore volume multiplier is applied, indicating gas that has escaped to regions far beyond the area of interest. The "Caprock" label accounts for the total amount of CO_2 or H_2 that has penetrated into the caprock layers (ESF), highlighting upward migration into low-permeability regions. The terms "Immobile", "Dissolved", and "Free" represent their respective amounts within the porous part of the medium, excluding the cap rock and PVM cells.

Similar to the standard conditions (STC) case, the first notable difference is the significantly higher dissolution of CO_2 compared to H_2. CO_2 continues dissolving over time through the previously discussed dissolution-sinking process, drawing from both the free CO_2 and immobile CO_2. It is anticipated that the dissolved amount of CO_2 would be substantially higher in a larger reservoir, as the R_s distribution (Fig.

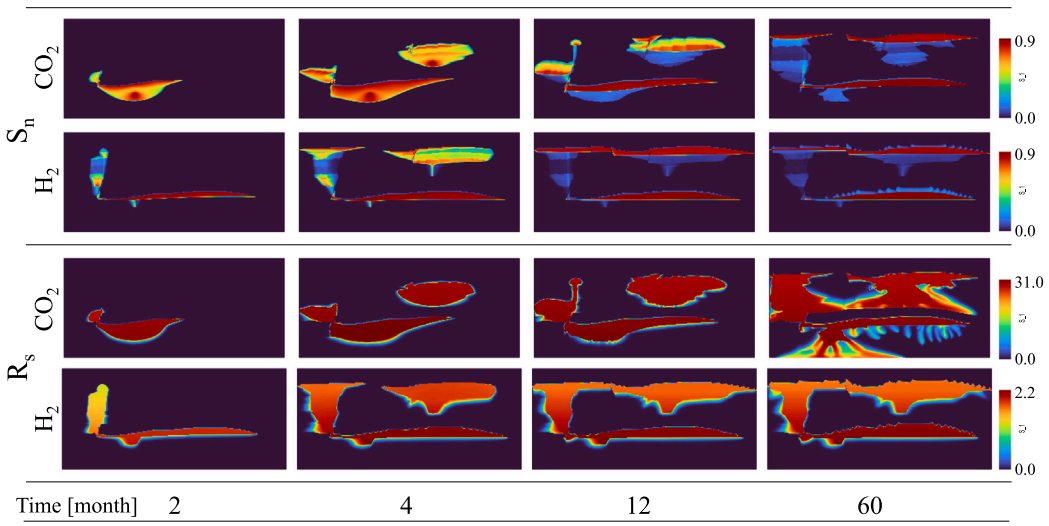

Fig. 8. A comparison between the evolution over time of the spatial distribution of nonwetting phase saturation, S_n, and dissolution, R_s, for the CO_2 and H_2 cases at reservoir conditions.

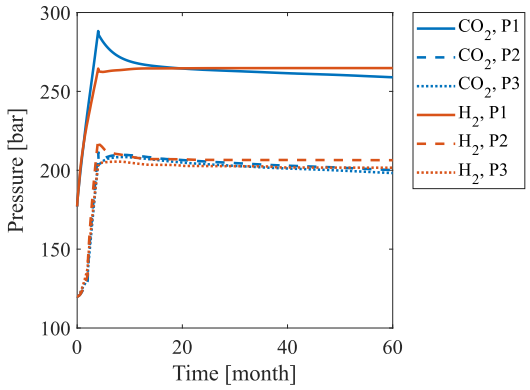

Fig. 9. A comparison between nonwetting phase pressure, p_n, at points P1, P2, and P3 for the CO_2 and H_2 cases.

8) indicates that the water is saturated with dissolved CO_2 throughout the domain.

The amount of immobile CO_2 is greater than that of H_2, primarily due to the broader and more dispersed shape of the CO_2 plume, which allows it to occupy a larger spatial area compared to the H_2 plume. In contrast, the higher penetration of H_2 into the caprock is evident, with values exceeding those of CO_2 by more than a factor of three. Additionally, approximately 5% of the injected CO_2 and 12% of the injected H_2 escape the domain after 5 years. The higher escape fraction of H_2 and its continuation even after 5 years are attributed to its greater mobility.

These observations emphasize the critical role of structural trapping for UHS. While CO_2 storage is primarily influenced by dissolution, for H_2, the contributions of "Escaped", "Caprock", and "Immobile" mass fractions are just as significant as dissolution. Another key point is that CO_2, due to its broader plume shape, can reach more regions and encounter more fractures, whereas H_2, despite covering less area, escapes much faster through fractures.

It should be emphasized that although the solubility of H_2 under reservoir conditions is comparable to that of CO_2 under standard conditions, the overall solubility of both CO_2 and H_2 in reservoir conditions remains low (see Fig. 6 for CO_2 compared to Fig. 10(a)). This is because solubility is not the sole factor influencing dissolution trapping. Other crucial factors include the water-to-injected-gas ratio (i.e., having sufficient water) and the dissolution-sinking process, as fingering. In reservoir conditions, these fingers are significantly larger, requiring more space and time to fully develop and sink.

3.2.1. Effect of salinity

Salinity can play an important role in determining the behavior and efficiency of subsurface storage in saline aquifers. It directly impacts the solubility of the injected gas in water, with higher salinity levels reducing gas solubility, Fig. 1(c). This reduction in solubility lowers the capacity of highly saline reservoirs to store CO_2 effectively; however, it is beneficial for H_2 storage, as higher salinity reduces the amount of H_2 that dissolves into the water, minimizing losses. For example, in offshore environments, the initial salt concentration typically starts at $35\,g\,L^{-1}$ NaCl (or 35,000 ppm), which corresponds to the salinity of seawater. However, at a depth of approximately 2 km, salinity levels can rise significantly, reaching around $130\,g\,L^{-1}$, reflecting a gradient of approximately $50\,ppm\,m^{-1}$ [65,66]. This gradient can vary slightly depending on regional geological factors, such as the presence of salt tectonics, which may further influence local salinity distribution. For onshore reservoirs, salinity levels are even more variable and highly dependent on the geological history and hydrogeological conditions of the basin. In this section, the previous problem of plume migration in reservoir conditions is studied in the presence of salinity; two cases of a saline aquifer with a salinity of 1.1×10^5 ppm, and an extreme case of 3.0×10^5 ppm are studied.

Fig. 10(b) illustrates the mass fraction distribution of CO_2 and H_2 after 5 years for different salinity levels. The decrease in the total dissolved CO_2 and H_2 in the extreme salinity case compared to the non-salinity case is 11.9% and 1.25%, respectively. Salinity has a noticeable impact on the performance of CO_2 storage, primarily due to its substantial effect on CO_2 dissolution.

3.3. Cyclic storage

In this section a case of a cyclic storage is studied. The cyclic injection and production case is studied to better understand the dynamic behavior of CO_2 and H_2 during storage and retrieval operations, which are critical for real-world applications of subsurface storage. Cyclic operations introduce pressure fluctuations and repeated changes in gas saturation, which can influence plume migration, dissolution, and phase behavior. For H_2 storage, understanding recovery efficiency is particularly important, as H_2 losses through structural escape, dissolution, or escape through caprock could impact its viability.

Here, CO_2 and H_2 are stored beneath the top caprock layer from the previous case, and the upper 770 m section of the reservoir is modeled.

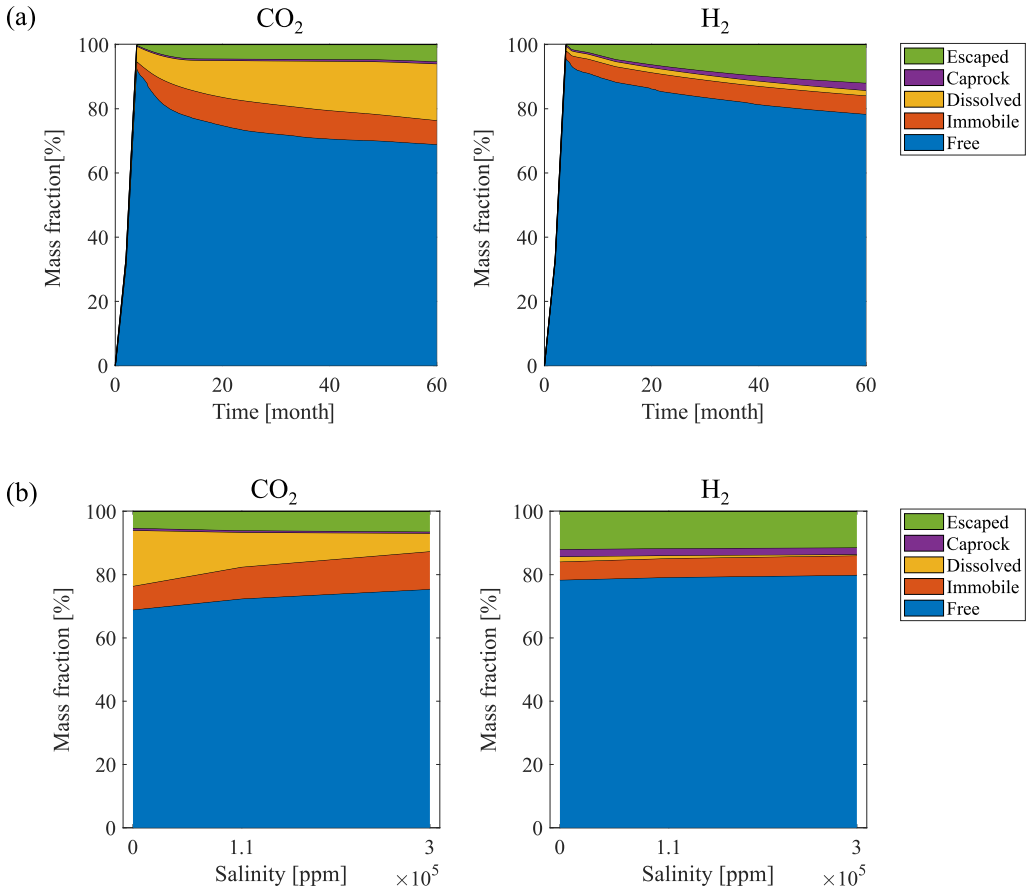

Fig. 10. A comparison of the mass fraction distribution of CO_2 and H_2 with respect to total injected mass at reservoir conditions. (a) The variations with time of the case with no salinity (b) The variations with salinity of the mass fraction distribution after 5 years.

Since the geometry of the FluidFlower consists of more parallel lateral layers, which are not suitable for structural trapping in cyclic storage (more than 10% escape is observed in the previous section), a barrier with no-flow boundary condition is indicated at the sides of layers "C" and "D" while a pore volume multiplier is applied only to layers "E", "F", and "G" to prevent unrealistic pressure build-up. The injection/production well is located at P2, starting with an injection phase at a rate of $580\,m^3\,s^{-1}$ for 3 months, followed by a 3-month idle period, a 3-month production phase at a controlled pressure of 108 bar (90% of the initial hydrostatic pressure at P2, to get the maximum producible CO_2 or H_2 and preserve well stability), and another 3-month idle phase. Each cycle spans one year, and the simulations are conducted over five complete cycles, providing a detailed analysis of cyclic storage dynamics.

Fig. 11 presents the spatial distribution of nonwetting phase saturation and dissolution for CO_2 and H_2 at the end of the injection and production period of the first and last cycles. While the overall size of the CO_2 and H_2 plumes appears comparable, the H_2 plume demonstrates a stronger tendency to spread horizontally within the reservoir. In both cases, because not all of the injected gas is produced during the cycles, the plume size increases over time. Notably, differences emerge in the shape of the plumes at the end of the production period. During the production phase in both cases, gases from below the well tend to be extracted earlier than those from the surrounding horizontal regions. This leads to the formation of a W-shaped plume. While CO_2 retains this W-shape after production, H_2 is produced and stabilizes more quickly. As a result, a larger volume of CO_2 remains trapped, reducing its recoverability. Regarding the R_s values, the dissolved gases maintain a similar spatial extent even after production phases, although the total quantity of dissolved CO_2 or H_2 decreases by the end of each cycle compared to when the reservoir is fully saturated following injection. This highlights the persistence of dissolved gases in the wetting phase despite cyclic extraction.

Fig. 12(a) compares the mass fraction distribution of CO_2 and H_2 within the domain with respect to the total injected mass during the first cycle. A general increase in all quantities is observed during injection periods, followed by a decrease during production periods. While CO_2 and H_2 initially exhibit the same mass fraction of free gas at the end of the first injection, the following cycles show an increase in free CO_2 within the reservoir, whereas the amount of free H_2 converges. This difference is attributed to CO_2's lower mobility, which leads to reduced recoverability (Fig. 12(b)), resulting in a portion of CO_2 remaining trapped in the reservoir. The results indicate that H_2 has a high recoverability rate, achieving more than 95% recovery after the first cycle.

Dissolved CO_2 shows a continuously increasing trend across cycles, whereas dissolved H_2 remains relatively constant in both pattern and quantity throughout all cycles. This contrast is also evident in the spatial distribution of R_s (Fig. 11), where the extent of dissolved CO_2 has expanded significantly by the end of the fifth cycle compared to the first.

The amount of immobile gas during the injection period does not follow a simple pattern. While the plume expands during injection (leading to an increase in immobile gas amount, as well), previously trapped gas can also become reconnected and mobilized, offsetting this increase. However, during the idle phase following injection, buoyancy-driven upward migration can further reconnect and mobilize trapped gas, leading to a noticeable decrease in immobile gas—an effect that

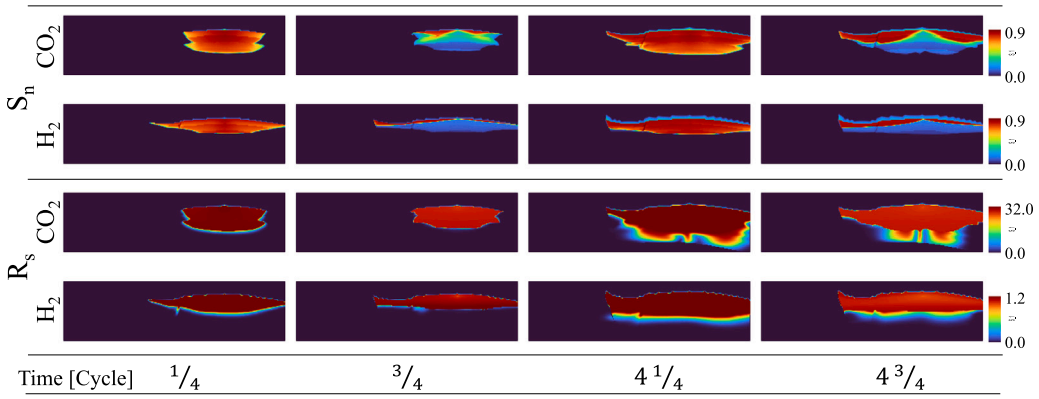

Fig. 11. A comparison between the evolution over time of the spatial distribution of nonwetting phase saturation, S_n, and dissolution, R_s, for the CO_2 and H_2 cases in cyclic storage case.

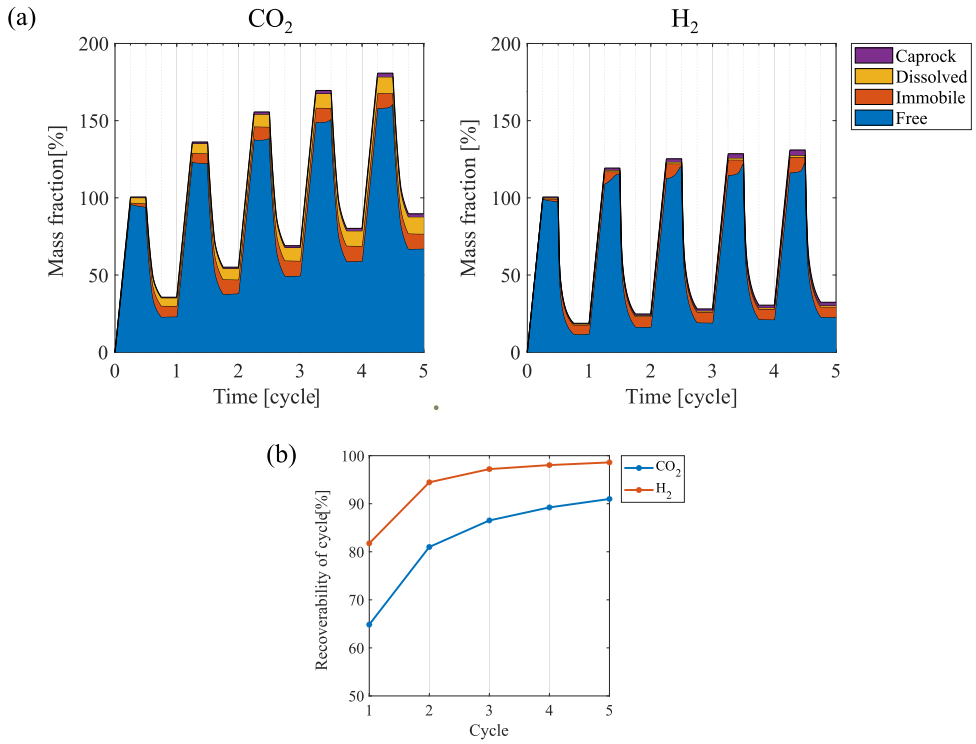

Fig. 12. (a) A comparison of the mass fraction distribution of the CO_2 and H_2 cases with respect to the total injected mass in the first cycle and (b) The recoverability of each cycle at cyclic storage case.

is more pronounced in the case of H_2 due to its higher mobility and buoyancy. Following the production phase, both CO_2 and H_2 show a clear increase in immobile gas, as the reservoir undergoes imbibition and a large portion of the gas becomes residually trapped.

The amount of gas withdrawn from the caprock during production is less than the amount that enters (similar to other parts of the reservoir). Consequently, with each cycle, more gas accumulates within the caprock. This effect is more pronounced for H_2 due to its higher Bond number. As the entry capillary pressure is exceeded at multiple points, it becomes easier for H_2 to migrate deeper into the caprock. The nonwetting phase initially invades the largest pores. As pressure increases, it progressively invades smaller pores, further advancing its penetration. In cyclic storage systems, the pressure fluctuations near the caprock caused by frequent injection and withdrawal can gradually weaken the caprock's sealing capacity, thereby increasing the risk of leakage over time.

4. Practical insights

This section presents key insights found from the comparative analyses and how these findings can be translated into practical real-field applications for cyclic hydrogen storage (UHS) and permanent CO_2 disposal (GCS) projects.

It is evident that the thermophysical properties of CO_2 and H_2 differ significantly, leading to distinct plume migration patterns and trapping. Interestingly, these differing properties are advantageous within the context of their respective storage applications. The higher solubility of CO_2 promotes greater dissolution trapping in the aquifer, and its higher density leads to gravitational fingering, further enhancing dissolution over time. In contrast, the high mobility of H_2 improves its productivity during withdrawal of gas, while its low solubility minimizes dissolution losses, thereby preserving more of the injected gas for recovery.

Reservoir geometry and structural geology play crucial roles in site selection for each application. For CCS, aiming to permanently

store CO_2, big reservoirs which allow for CO_2 plume to spread over larger volumes is advantageous. This is because the more spreading of the plume, the higher the residual and dissolution trapping. In UHS, however, minimizing the plume spreading and its associated losses is essential. Therefore, structurally confined traps — preferably with steeper dips — are required to limit lateral spreading and gravity override. Additionally, selecting a reservoir with an optimized size that matches the desired storage capacity of the project helps to reduce unnecessary plume extension and improve containment efficiency.

Heterogeneity in porosity, permeability, and capillary pressure influences plume shape and extent. In the context of CCS, such heterogeneity can be advantageous, as it may lead to longer migration pathways and more permanent trapping. However, for UHS, it is less desirable, as an uneven plume distribution may result in lower recovery factors.

Sealing integrity, comprising the caprock, wellbores, legacy wells, and side-sealing faults, is crucial for structural trapping in both storage systems. However, due to the high mobility and buoyancy of H_2, even minor leakage pathways in UHS can result in significant losses. Although H_2 exhibits higher interfacial tension under reservoir conditions, its lower density leads to a higher Bond number compared to CO_2. This enhances the H_2 penetrations into the caprock. As a result, it is essential to carefully select a high-integrity caprock for UHS, i.e., with low permeability and high capillary entry pressure, and to maintain reservoir pressure below this threshold. If the pressure exceeds the capillary entry pressure, the gas can gradually form pathways through the caprock over time and repeated cycles, increasing the risk of leakage. Moreover, frequent injection and withdrawal cycles induce pressure fluctuations near the caprock. These fluctuations can progressively promote gas invasion into the caprock, ultimately compromising its sealing effectiveness. Consequently, continuous monitoring of hydrogen loss, directly or indirectly via e.g. pressure distribution, is crucial.

Generally, salinity reduces the dissolution of gases in brine. For GCS, since dissolution trapping is essential, the salinity distribution of the reservoir over depth should be carefully considered for site selection and storage capacity estimation. Since the dissolution of H_2 in brine is not significant, other negative effects of salinity, like salt precipitation, is more relevant to be considered for site selection and performance analyses.

During H_2 withdrawal in UHS, a W-shaped plume is observed because gas near the wellbore is produced more easily and rapidly than the gas located farther away. This uneven extraction leads to complex fluid distribution, ultimately resulting in incomplete gas recovery. To address this, strategies such as optimizing the number and their associated rates can help achieve higher recovery factors. More precisely, producing at a lower rate over a longer period, if possible, can help enable plume stabilization and significantly enhance recoverability. Note that such analyses for well configurations and operational conditions need to also include the specific reservoir geometry and its permeability heterogeneity and anisotropy.

5. Conclusions

This study presented a comprehensive comparative analysis of CO_2 and H_2 plume migration in geological formations, highlighting critical differences in their flow patterns, trapping mechanisms, dissolution, escaping, and caprock integrity.

Consistent with the literature [46], our study confirmed that H_2 exhibits higher mobility than CO_2 due to its lower viscosity. As a result, H_2 migrates upward in permeable regions, accumulates in a horizontal configuration beneath the caprock. As a result in well-structured geometries (with limited or no escape pathways) its plume reaches a steady state configuration much more quickly than that of CO_2. In standard conditions, H_2 can form a larger plume because a significant portion of the CO_2 plume dissolves into the brine. Additionally, H_2 can escape through fractures faster and reaches farther distances, whereas a significant portion of CO_2 that penetrates through fractures dissolves along the way.

Moreover, it was found that a significant portion of CO_2 dissolves into the brine, reducing its presence in the nonwetting phase. In contrast, H_2 cases generally exhibit higher pressures within the medium due to the larger spatial occupancy of the nonwetting (compressed gas) phase. This elevated pressure in H_2 cases results in greater chances of leakage, both in terms of rate and duration through fractures or migration to distant regions (e.g. legacy wells). However, exceptions can arise when leakage of H_2 plume through a fracture reduces the local pressure, or when the geometry of the CO_2 plume enables it to access fractures that the H_2 plume could not reach.

In H_2 cases, higher pressure values combined with greater buoyancy forces can lead to increased chances of penetration into the caprock. Although H_2 exhibits higher interfacial tension — and consequently a higher threshold capillary pressure — under reservoir conditions, its greater buoyancy results in a higher Bond number compared to CO_2. As demonstrated in the literature [67], and confirmed by our simulations, once leakage into the caprock begins, H_2 is expected to escape more rapidly due to its channeling flow pattern.

Furthermore, dissolution trapping in geological formations is a function of solubility, the injected gas to reservoir size ratio, and the sinking (or dynamic transport) of the dissolved gas within the brine. The gravity-driven fingering of CO_2 spreads its concentration through the brine, and makes space for more CO_2 to be dissolved through time. As a result of H_2's lower density, there is no apparent gravity-driven fingering in the its plume; thus, the dissolved H_2 concentration spreads evenly near the gas–liquid contact surface, which is beneficial since it limits its solubility and increases its recoverability.

Finally, in cyclic storage, over many cycles, the plume size increases due to the spreading of the non-recoverable gas. It is observed that H_2 plume stabilized much faster horizontally, due to its higher mobility, while CO_2 plume retains a W-shape configuration for a longer period of time. The lower mobility of CO_2 increases its trapped volumes in the reservoir, decreasing its recoverability. Through cycles, dissolved CO_2 exhibits a continuously increasing trend, whereas dissolved H_2 remains relatively constant in both pattern and quantity throughout all cycles, which is beneficial for that it minimizes its solubility loss after the first cycle. In the cyclic case, H_2 again preserves its higher penetration rates through the caprock than CO_2. Note that the comparison between H_2 and CO_2 is only made for better characterization of the H_2 plume dynamics in the reservoir, as some of their distinct features, as clarified in this work, helps for a robust design of an efficient system for each.

CRediT authorship contribution statement

Amin Misaghi Bonabi: Writing – original draft, Visualization, Software, Methodology, Investigation, Formal analysis, Conceptualization. **Willemijn van Rooijen:** Writing – original draft, Software, Methodology. **Mohammed Al Kobaisi:** Writing – review & editing, Conceptualization. **Cornelis Vuik:** Writing – review & editing, Supervision, Conceptualization. **Hadi Hajibeygi:** Writing – review & editing, Supervision, Methodology, Funding acquisition, Conceptualization.

Declaration of competing interest

The authors declare that they have no known competing financial interests or personal relationships that could have appeared to influence the work reported in this paper.

Acknowledgments

The authors acknowledge the funding of the European Union's Horizon Europe Research and Innovation programme under Marie Skłodowska-Curie for Doctoral Training Network (EU ITN) project "SHINE" with the Grant Agreement No. 101073271. All implementations are made available to public in the open-source Delft Advanced Reservoir Simulator (DARSim) [48].

References

[1] Krevor Samuel, De Coninck Heleen, Gasda Sarah E, Ghaleigh Navraj Singh, de Gooyert Vincent, Hajibeygi Hadi, Juanes Ruben, Neufeld Jerome, Roberts Jennifer J, Swennenhuis Floris. Subsurface carbon dioxide and hydrogen storage for a sustainable energy future. Nat Rev Earth Environ 2023;4(2):102–18.

[2] Metz Bert, Davidson Ogunlade, De Coninck HC, Loos Manuela, Meyer Leo. IPCC special report on carbon dioxide capture and storage. Technical report, Cambridge: Cambridge University Press; 2005.

[3] Bui Mai, Adjiman Claire S, Bardow André, Anthony Edward J, Boston Andy, Brown Solomon, Fennell Paul S, Fuss Sabine, Galindo Amparo, Hackett Leigh A, et al. Carbon capture and storage (CCS): the way forward. Energy Environ Sci 2018;11(5):1062–176.

[4] Tashie-Lewis Bernard Chukwudi, Nnabuife Somtochukwu Godfrey. Hydrogen production, distribution, storage and power conversion in a hydrogen economy-a technology review. Chem Eng J Adv 2021;8:100172.

[5] Abe John O, Popoola API, Ajenifuja Emmanueal, Popoola Olawale M. Hydrogen energy, economy and storage: Review and recommendation. Int J Hydrog Energy 2019;44(29):15072–86.

[6] Berrezueta Edgar, Kovács Timea, Herrera-Franco Gricelda, Caicedo-Potosí Jhon, Jaya-Montalvo María, Ordóñez Casado Berta, Carneiro Júlio. Laboratory studies on underground H_2 storage: Bibliometric analysis and review of current knowledge. Technical report, Hydrogen Knowledge Centre; 2024.

[7] Sorensen Bent. Hydrogen and fuel cells: emerging technologies and applications. Academic Press; 2011.

[8] Hydrogen TCP. Task 42, Underground hydrogen storage: Technology monitor report. Technical report, International Energy Agency; 2023.

[9] Zivar Davood, Kumar Sunil, Foroozesh Jalal. Underground hydrogen storage: A comprehensive review. Int J Hydrog Energy 2021;46(45):23436–62.

[10] Shojaee A, Ghanbari S, Wang G, Mackay E. Interplay between microbial activity and geochemical reactions during underground hydrogen storage in a seawater-rich formation. Int J Hydrog Energy 2024;50:1529–41.

[11] Heinemann Niklas, Alcalde Juan, Miocic Johannes M, Hangx Suzanne JT, Kallmeyer Jens, Ostertag-Henning Christian, Hassanpouryouzband Aliakbar, Thaysen Eike M, Strobel Gion J, Schmidt-Hattenberger Cornelia, et al. Enabling large-scale hydrogen storage in porous media–the scientific challenges. Energy Environ Sci 2021;14(2):853–64.

[12] Rezaei Amin, Hassanpouryouzband Aliakbar, Molnar Ian, Derikvand Zeinab, Haszeldine R Stuart, Edlmann Katriona. Relative permeability of hydrogen and aqueous brines in sandstones and carbonates at reservoir conditions. Geophys Res Lett 2022;49(12):e2022GL099433.

[13] Thaysen Eike M, Jangda Zaid, Hassanpouryouzband Aliakbar, Menke Hannah, Singh Kamaljit, Butler Ian B, Heinemann Niklas, Edlmann Katriona. Hydrogen wettability and capillary pressure in Clashach sandstone for underground hydrogen storage. J Energy Storage 2024;97:112916.

[14] Van Rooijen WA, Habibi P, Xu K, Dey P, Vlugt TJH, Hajibeygi H, Moultos OA. Interfacial tensions, solubilities, and transport properties of the H_2/H_2O/NaCl system: A molecular simulation study. J Chem Eng Data 2023;69(2):307–19.

[15] Hassanpouryouzband Aliakbar, Joonaki Edris, Edlmann Katriona, Heinemann Niklas, Yang Jinhai. Thermodynamic and transport properties of hydrogen containing streams. Sci Data 2020;7(1):222.

[16] Adam Abdelateef M, Bahamon Daniel, Al Kobaisi Mohammed, Vega Lourdes F. Molecular dynamics simulations of the interfacial tension and the solubility of brine/H_2/CO_2 systems: Implications for underground hydrogen storage. Int J Hydrog Energy 2024;78:1344–54.

[17] Hulikal Chakrapani Thejas, Hajibeygi Hadi, Moultos Othonas A, Vlugt Thijs JH. Mutual diffusivities of mixtures of carbon dioxide and hydrogen and their solubilities in brine: Insight from molecular simulations. Ind Eng Chem Res 2024.

[18] Hashemi Leila, Glerum Wuis, Farajzadeh Rouhi, Hajibeygi Hadi. Contact angle measurement for hydrogen/brine/sandstone system using captive-bubble method relevant for underground hydrogen storage. Adv Water Resour 2021;154:103964.

[19] Hashemi Leila, Boon Maartje, Glerum Wuis, Farajzadeh Rouhi, Hajibeygi Hadi. A comparative study for H_2–CH_4 mixture wettability in sandstone porous rocks relevant to underground hydrogen storage. Adv Water Resour 2022;163:104165.

[20] Lysyy Maksim, Liu Na, Solstad Celine M, Fernø Martin A, Ersland Geir. Microfluidic hydrogen storage capacity and residual trapping during cyclic injections: Implications for underground storage. Int J Hydrog Energy 2023;48(80):31294–304.

[21] Ali Muhammad, Yekeen Nurudeen, Pal Nilanjan, Keshavarz Alireza, Iglauer Stefan, Hoteit Hussein. Influence of pressure, temperature and organic surface concentration on hydrogen wettability of caprock; implications for hydrogen geo-storage. Energy Rep 2021;7:5988–96.

[22] Mouallem Johny, Arif Muhamad, Raza Arshad, Glatz Guenther, Rahman Md Motiur, Mahmoud Mohamed, Iglauer Stefan. Critical review and meta-analysis of the interfacial tension of CO_2-brine and H_2-brine systems: Implications for CO_2 and H_2 geo-storage. Fuel 2024;356:129575.

[23] Chow YT Florence, Maitland Geoffrey C, Trusler JP Martin. Interfacial tensions of (H_2O+ H_2) and (H_2O+ CO_2+ H_2) systems at temperatures of (298–448) K and pressures up to 45 MPa. Fluid Phase Equilib 2018;475:37–44.

[24] Hosseini Mirhasan, Fahimpour Jalal, Ali Muhammad, Keshavarz Alireza, Iglauer Stefan. H_2- brine interfacial tension as a function of salinity, temperature, and pressure; implications for hydrogen geo-storage. J Pet Sci Eng 2022;213:110441.

[25] Boon Maartje, Hajibeygi Hadi. Experimental characterization of H_2/water multiphase flow in heterogeneous sandstone rock at the core scale relevant for underground hydrogen storage (UHS). Sci Rep 2022;12(1):14604.

[26] Thaysen Eike M, Butler Ian B, Hassanpouryouzband Aliakbar, Freitas Damien, Alvarez-Borges Fernando, Krevor Samuel, Heinemann Niklas, Atwood Robert, Edlmann Katriona. Pore-scale imaging of hydrogen displacement and trapping in porous media. Int J Hydrog Energy 2023;48(8):3091–106.

[27] Higgs Scott, Da Wang Ying, Sun Chenhao, Ennis-King Jonathan, Jackson Samuel J, Armstrong Ryan T, Mostaghimi Peyman. In-situ hydrogen wettability characterisation for underground hydrogen storage. Int J Hydrog Energy 2022;47(26):13062–75.

[28] Higgs Scott, Da Wang Ying, Sun Chenhao, Ennis-King Jonathan, Jackson Samuel J, Armstrong Ryan T, Mostaghimi Peyman. Direct measurement of hydrogen relative permeability hysteresis for underground hydrogen storage. Int J Hydrog Energy 2024;50:524–41.

[29] Boon Maartje, Rademaker Tim, Winardhi Chandra Widyananda, Hajibeygi Hadi. Multiscale experimental study of H2/brine multiphase flow in porous rock characterizing relative permeability hysteresis, hydrogen dissolution, and Ostwald ripening. Sci Rep 2024;14(1):1–15.

[30] Goodarzi Sepideh, Zhang Yihuai, Foroughi Sajjad, Bijeljic Branko, Blunt Martin J. Trapping, hysteresis and Ostwald ripening in hydrogen storage: A pore-scale imaging study. Int J Hydrog Energy 2024;56:1139–51.

[31] Yekta AE, Manceau J-C, Gaboreau Stéphane, Pichavant Michel, Audigane Pascal. Determination of hydrogen–water relative permeability and capillary pressure in sandstone: application to underground hydrogen injection in sedimentary formations. Transp Porous Media 2018;122(2):333–56.

[32] Lysyy Maksim, Føyen Tore, Johannesen Else Birkeland, Fernø Martin, Ersland Geir. Hydrogen relative permeability hysteresis in underground storage. Geophys Res Lett 2022;49(17):e2022GL100364.

[33] Boon Maartje, Buntic Ivan, Ahmed Kadir, Dopffel Nicole, Peters Catherine, Hajibeygi Hadi. Microbial induced wettability alteration with implications for underground hydrogen storage. Sci Rep 2024;14(1):8248.

[34] Alkan Hakan, Szabries Martina, Dopffel Nicole, Koegler Felix, Baumann Roelf-Peter, Borovina Ante, Amro Mohd. Investigation of spontaneous imbibition induced by wettability alteration as a recovery mechanism in microbial enhanced oil recovery. J Pet Sci Eng 2019;182:106163.

[35] Liu Na, Kovscek Anthony R, Fernø Martin A, Dopffel Nicole. Pore-scale study of microbial hydrogen consumption and wettability alteration during underground hydrogen storage. Front Energy Res 2023;11:1124621.

[36] Hashemi Leila, Blunt Martin, Hajibeygi Hadi. Pore-scale modelling and sensitivity analyses of hydrogen-brine multiphase flow in geological porous media. Sci Rep 2021;11(1):8348.

[37] Wang Yuhang, Chakrapani Thejas Hulikal, Wen Zhang, Hajibeygi Hadi. Pore-scale simulation of H2-brine system relevant for underground hydrogen storage: A lattice Boltzmann investigation. Adv Water Resour 2024;104756.

[38] Bi Zhenhui, Guo Yintong, Yang Chunhe, Yang Hanzhi, Wang Lei, He Yuting, Guo Wuhao. Numerical investigation of fluid dynamics in aquifers for seasonal large-scale hydrogen storage using compositional simulations. Renew Energy 2025;239:122101.

[39] Zhao Qingqi, Wang Yuhang, Chen Cheng. Numerical simulation of the impact of different cushion gases on underground hydrogen storage in aquifers based on an experimentally-benchmarked equation-of-state. Int J Hydrog Energy 2024;50:495–511.

[40] Ahmed Elyes, Møyner Olav, Raynaud Xavier, Nilsen Halvor M. Phase behavior and black-oil simulations of hydrogen storage in saline aquifers. Adv Water Resour 2024;191:104772.

[41] Bo Zhenkai, Boon Maartje, Hajibeygi Hadi, Hurter Suzanne. Impact of experimentally measured relative permeability hysteresis on reservoir-scale performance of underground hydrogen storage (UHS). Int J Hydrog Energy 2023;48(36):13527–42.

[42] Belhaj H, Rodriguez F, Askarova AA, Bejarano C, Morales R, AlDhuhoori M, Alekhina TV, Dorhjie DB, Spivakova MY, Mukhametova AR, et al. Modeling hydrogen storage in El Carito-Mulata and Santa Barbara Fields, eastern Venezuela Basin: Focus on the cushion gas effect and identification of recovery mechanisms. In: SPE annual technical conference and exhibition. SPE; 2024, D031S045R002.

[43] Luboń Katarzyna, Tarkowski Radosław. Numerical simulation of hydrogen injection and withdrawal to and from a deep aquifer in NW Poland. Int J Hydrog Energy 2020;45(3):2068–83.

[44] Zamehrian Mohammad, Sedaee Behnam. Underground hydrogen storage in a partially depleted gas condensate reservoir: influence of cushion gas. J Pet Sci Eng 2022;212:110304.

[45] Wang G, Pickup G, Sorbie K, Mackay E. Numerical modelling of H_2 storage with cushion gas of CO_2 in subsurface porous media: Filter effects of CO_2 solubility. Int J Hydrog Energy 2022;47(67):28956–68.

[46] Pan Bin, Liu Kai, Ren Bo, Zhang Mingshan, Ju Yang, Gu Jianwei, Zhang Xueying, Clarkson Christopher R, Edlmann Katriona, Zhu Weiyao, et al. Impacts of relative permeability hysteresis, wettability, and injection/withdrawal schemes on underground hydrogen storage in saline aquifers. Fuel 2023;333:126516.
[47] Flemisch Bernd, Nordbotten Jan M, Fernø Martin, Juanes Ruben, Both Jakub W, Class Holger, Delshad Mojdeh, Doster Florian, Ennis-King Jonathan, Franc Jacques. The FluidFlower validation benchmark study for the storage of CO_2. Transp Porous Media 2024;151(5):865–912.
[48] Darsim (Delft Advanced Reservoir Simulator). 2024, URL https://gitlab.com/darsim.
[49] Peng Ding-Yu, Robinson Donald B. A new two-constant equation of state. Ind Eng Chem Fundam 1976;15(1):59–64.
[50] Mathias Paul M, Naheiri Tarik, Oh Edwin M. A density correction for the Peng—Robinson equation of state. Fluid Phase Equilib 1989;47(1):77–87.
[51] Ziabakhsh-Ganji Zaman, Kooi Henk. An equation of state for thermodynamic equilibrium of gas mixtures and brines to allow simulation of the effects of impurities in subsurface CO_2 storage. Int J Greenh Gas Control 2012;11:S21–34.
[52] Spycher Nicolas, Pruess Karsten, Ennis-King Jonathan. CO_2-H_2O mixtures in the geological sequestration of CO_2. I. Assessment and calculation of mutual solubilities from 12 to 100 C and up to 600 bar. Geochim Cosmochim Acta 2003;67(16):3015–31.
[53] Quiñones-Cisneros Sergio E, Zéberg-Mikkelsen Claus K, Stenby Erling H. The friction theory (f-theory) for viscosity modeling. Fluid Phase Equilib 2000;169(2):249–76.
[54] Zéberg-Mikkelsen Claus K, Quiñones-Cisneros Sergio E, Stenby Erling H. Viscosity modeling of light gases at supercritical conditions using the friction theory. Ind Eng Chem Res 2001;40(17):3848–54.
[55] Lemmon Eric W, Bell Ian H, Huber ML, McLinden MO. NIST standard reference database 23: reference fluid thermodynamic and transport properties-REFPROP, version 10.0, National Institute of Standards and Technology. Stand Ref Data Program Gaithersburg 2018.
[56] Hassanzadeh Hassan, Pooladi-Darvish Mehran, Elsharkawy Adel M, Keith David W, Leonenko Yuri. Predicting PVT data for CO_2–brine mixtures for black-oil simulation of CO_2 geological storage. Int J Greenh Gas Control 2008;2(1):65–77.
[57] Wang Yuhang, Vuik Cornelis, Hajibeygi Hadi. Analysis of hydrodynamic trapping interactions during full-cycle injection and migration of CO_2 in deep saline aquifers. Adv Water Resour 2022;159:104073.
[58] Shabani Babak, Vilcáez Javier. TOUGHREACT-CO_2Bio–A new module to simulate geological carbon storage under biotic conditions (part 1): The multiphase flow of CO_2-CH_4-H_2-H_2S gas mixtures. J Nat Gas Sci Eng 2019;63:85–94.
[59] Torín-Ollarves Geraldine A, Trusler JP Martin. Solubility of hydrogen in sodium chloride brine at high pressures. Fluid Phase Equilib 2021;539:113025.
[60] Chabab Salaheddine, Théveneau Pascal, Coquelet Christophe, Corvisier Jérôme, Paricaud Patrice. Measurements and predictive models of high-pressure H_2 solubility in brine (H_2O+ NaCl) for underground hydrogen storage application. Int J Hydrog Energy 2020;45(56):32206–20.
[61] H2toolbox. 2024, https://gitlab.tudelft.nl/ADMIRE_Public/h2toolbox. [Accessed 08 April 2025].
[62] Pinder George F, Gray William G. Essentials of multiphase flow and transport in porous media. John Wiley & Sons; 2008.
[63] Wang Yuhang, Zhang Ziliang, Vuik Cornelis, Hajibeygi Hadi. Simulation of CO_2 storage using a parameterization method for essential trapping physics: FluidFlower benchmark study. Transp Porous Media 2024;151(5):1053–70.
[64] Abdoulghafour Halidi, Sarmadivaleh Mohammad, Hauge Lars Petter, Fernø Martin, Iglauer Stefan. Capillary pressure characteristics of CO_2-brine-sandstone systems. Int J Greenh Gas Control 2020;94:102876.
[65] Addassi Mouadh, Omar Abdirizak, Hoteit Hussein, Afifi Abdulkader M, Arkadakskiy Serguey, Ahmed Zeyad T, Kunnummal Noushad, Gislason Sigurdur R, Oelkers Eric H. Assessing the potential of solubility trapping in unconfined aquifers for subsurface carbon storage. Sci Rep 2022;12(1):20452.
[66] Steen AK, Nunn JA, Hanor JS. Indications of formation water flow and compartmentalization on the flank of a salt structure derived from salinity and seismic data. Geofluids 2011;11(2):199–208.
[67] Carden PO, Paterson Lincoln. Physical, chemical and energy aspects of underground hydrogen storage. Int J Hydrog Energy 1979;4(6):559–69.